Navier-Stokes Simulation of Burst Vortex Flowfields for Fighter Aircraft at High Incidence

Joseph Vadyak* and David M. Schuster†
Lockheed Aeronautical Systems Company, Marietta, Georgia 30063

A computational study has been conducted to investigate vortex breakdown on a generic fighter configuration operating at high incidence. The flow simulations are based on solutions of the full Reynolds-averaged Navier-Stokes equations using an implicit finite-difference algorithm. Results of the analysis have been correlated with an experimental data base obtained using a three-dimensional laser velocimeter system. Good correlation has been obtained between the analysis and the data base in terms of the vortex core path, crossflow velocity fields, and the approximate vortex breakdown onset location.

Introduction

THE utilization of leading-edge vortex flows to extend the performance envelope of swept-wing fighters is now commonplace. Two examples of this are the F-16 and F/A-18 aircraft. Each of these highly maneuverable fighters employs leading-edge vortex flows to control separation, increase lift, and provide stability throughout their high-angle-of-attack operational regimes. However, the exploitation of the positive effects of this type of vortical flow does not come without its drawbacks. Under certain conditions, the vortical flow becomes unstable and leads to breakdown, sometimes labelled "vortex burst."

The immediate effects of vortex burst are often seen as wing rock, adverse pitching moment, and buffet. As the members of the aircraft fleet continue to build operational hours while routinely flying in these regimes, the long-term effects of the vortical flowfield interacting with the airframe become apparent. As reported in Ref. 1, the F/A-18 aircraft has developed vertical stabilizer fatigue problems as a result of the airframe interaction with the vortices emanating from the wing leading-edge extensions (LEX).

Currently, this problem is being addressed by primarily experimental studies. In the recent water channel studies by Wentz, reported in Ref. 1, the unsteady nature of the LEX vortex-vertical stabilizer interaction was investigated for a 1/48 scale F/A-18. The studies showed that the characteristic frequencies found in the vertical stabilizer flow region were induced by the breakdown of the LEX vortex. Although highly informative, the studies need to be extended in both Reynolds number and Mach number so that the nature of the breakdown is determined and understood.

At the Vortex Flows Aerodynamics Conference sponsored by the Air Force and NASA Langley Research Center in 1985, such problems were recognized as being significant stumbling blocks for the current airframe designer. Campbell and Osborn[2] further elaborated by challenging computational fluid dynamics (CFD) method developers with the need for predicting vortex breakdown and the effects associated with it.

Efforts in computationally predicting vortex flowfields have been made by researchers using Euler equation solution methods and more recently Navier-Stokes equation solution techniques.[3-8] Most of these studies have been concerned with incidences low enough that vortex breakdown was not induced. However, Fujii and Schiff[6] have reported simulating vortical flows over a strake-delta wing at various incidences by solving the thin-layer Navier-Stokes equations. At sufficiently high incidence, their computations showed evidence of vortex breakdown.

To gain a better understanding of burst vortex flowfields, a combined computational/experimental investigation was performed, as described in this paper, for a straked/swept-wing generic fighter flowfield over an incidence range that produced both stable vortical flows (lower incidence) and unstable burst vortical flows (high incidence). The computational study is based on simulating the flowfield using the three-dimensional Reynolds-averaged Navier-Stokes equations. The experimental investigation was performed using a nonintrusive three-dimensional laser velocimeter (LV) to survey the vortical flow regions. The experimental investigation was conducted by Novak and Huie, and is discussed in detail in Ref. 9. The computational method and the resulting correlation with the experimental data base are described below.

Three-Dimensional Navier-Stokes Flow Analysis

A computer analysis, called ENS3D, has been developed for calculating steady (or unsteady) three-dimensional flowfields for a variety of aircraft components or complete integrated aircraft configurations.[13-16] The flowfield solution for a given configuration is determined on a body-fitted three-dimensional structured curvilinear computational mesh. The computational mesh for each different configuration is determined by a separate grid generation algorithm. Most of the mesh generation algorithms rely on numerical grid generation techniques that are based on solving a system of coupled elliptic partial differential equations. Isolated component geometries are typically analyzed using a single block grid approach. Multicomponent configurations are typically analyzed using a multiblock H-grid approach, where the global computational grid is composed of a series of Cartesian-like subgrids patched together along common interface boundaries.

Once the computational grid is generated, the flowfield is obtained using the ENS3D analysis by solving either the full three-dimensional Reynolds-averaged Navier-Stokes equations or simplified versions thereof, namely, the thin-shear-layer Navier-Stokes equations, or the Euler equations. The governing equations are cast in strong conservation-law form to admit solutions in which shocks are captured. Second-order differencing is used in computing the metric parameters that map the physical domain to the computational domain. A time-marching full-implicit approximate factorization scheme is used for solution of the finite-difference equations. Either steady-state or time-accurate solutions can be obtained, with

Presented as Paper 89-2190 at the AIAA 7th Applied Aerodynamics Conference, Seattle, WA, July 31-Aug. 2, 1989; received Aug. 28, 1989; revision received Oct. 8, 1990; accepted for publication Nov. 5, 1990.

*Senior Scientist; currently, Senior Research and Development Engineer, Lockheed Advanced Development Co., Burbank, CA. Member AIAA.

†Scientist; currently, Research Engineer, Georgia Tech Research Institute, Atlanta, GA. Member AIAA.

second- or fourth-order spatial accuracy and first- or second-order temporal accuracy. The convective (inviscid) terms in the governing equations are differenced using either central differencing or the upwind differencing scheme of Ref. 10. The upwind differencing option considers the range of influence and domain of dependence at a solution mesh point, and is often used for supersonic flow calculations. The viscous diffusion terms employ central differencing.

Although the interior points are updated implicitly, an explicit boundary condition treatment is employed that allows for the adaption of the program to new configurations. To aid convergence, nonreflecting subsonic outflow boundary conditions are employed along with a spatially varying time step for steady-flow solution cases. For the central difference option, the algorithm can use either a constant coefficient artificial dissipation model or a variable coefficient model, where the coefficient's magnitude is based on the local pressure gradient. For the upwind differencing option, the algorithm is naturally dissipative. Laminar viscosity is computed for viscous cases using Sutherland's law. For turbulent viscous flows, the effective eddy viscosity is currently computed using either the Baldwin-Lomax two-layer algebraic turbulence model,[11] or the k-ϵ two-equation transport model.[12] For cases with separation, a streamwise eddy viscosity relaxation scheme may also be used in conjunction with the Baldwin-Lomax turbulence model.

In an effort to reduce the required computer execution time, versions of the flow simulation analysis were developed for use on Class VI vector supercomputers. Vectorized and vectorized/multitasked versions of the program have been developed for CRAY X-MP and Y-MP supercomputers. The single processor CRAY Y-MP Navier-Stokes computation rate is 3.5×10^{-5} s per grid point per iteration.

Applications of this analysis to aircraft component flowfield simulations are presented in Refs. 13–16.

Description of Generic Fighter Configuration and Instrumentation

Geometry data from a scale drawing of a generic fighter configuration were used to produce a numerical model description suitable for both numerically controlled (NC) milling and CFD grid generation purposes. The wire frame representation of the geometry is shown in Fig. 1. To reduce the complexities in the geometry definition and difficulties during LV testing, the engine inlet region was blended over and the wing tip verticals were removed.

For fabrication purposes, a 0.035 scale loft was used to generate the subsequent NC milling tapes. With fabrication at this scale, the model was large enough to allow a six-component internal airloads balance to be placed within it with few additional machining operations. Furthermore, wind-tunnel blockage based on the models' frontal area at 20-deg angle of attack could be held to be less than 5% for the wind tunnel used in this study. The completed model has a span of 13.72 in. and an overall length of 18.0 in. The strake is swept at 76 deg and the wing, biconvex in sectional shape, has a tip thickness of 4% chord and a leading-edge sweep of 56 deg and trailing-edge sweep of 30 deg. Wing area, based on extending the leading- and trailing-edge sweep lines to the centerline of the model, was calculated to be 68.6 in.^{2}. For wind-tunnel installation, a sting and sector arrangement was designed and the mounting hardware constructed such that the model's mean aerodynamic center (MAC) remained centered in the test section at the center of the sidewall window. This facilitated the three-dimensional LV testing with an unobscured view of the model and its flowfield.

Experimental Testing Procedures

Testing was undertaken in the LASC low turbulence wind tunnel at a maximum wind-tunnel velocity of 150 ft/s (maintainable throughout model angle-of-attack range). The Reynolds number, based on tunnel freestream velocity and model centerline length, was $\sim 1.25 \times 10^6$. To seed the flowfield for the three-dimensional LV measurements, mineral oil, with particle diameters equal to or less than 1 μm, was employed. A separate investigation indicated this small seed particle size would allow accurate tracing by the particles in the vortical flow region.

Prior to making the velocity measurements, laser sheet lighting was also used to visualize vortex position so that data acquisition could be concentrated in the regions of interest. With the vortex position determined, tables of survey locations were then constructed. Each table consisted of approximately 300 separate x, y, z locations in the flowfield, all of which were contained in a plane normal (y-z plane) to the centerline of the model. At each of the survey planes, the fuselage/wing (x) station value was held constant. Flowfield comparisons at different angles of attack were made with the survey planes fixed to the model's coordinate system and the velocities rotated to the same frame of reference.

Data rates of approximately 200 valid velocity samples per second were typical when using the 1-μm-mean-diam mineral oil seeding material. At each acquisition position, 1000 velocity samples were acquired such that the mean velocity and limited high-order moments could be constructed. The total time for data acquisition and positioning per wing chord station was approximately 2–3 h.

The uncertainty in the estimation of the mean transverse (W) velocity was approximately 5% for a standard deviation of 100 ft/s. This represented a "worst case" situation. For other regions in the flowfield, the standard deviations measured were in the 25–50 ft/s range. Hence, uncertainties in velocity are estimated at 1–3% in the longitudinal and vertical directions (U and V) and 2–5% in the transverse (W) direction. Positioner errors are based on the uncertainty in physically repositioning the laser beams on the "home" position located on the model's centerline. The least crucial of those was the x direction, with a value estimated at $\pm$ 0.007 in. The estimated uncertainties in the y and z directions are 0.005–0.010 in.

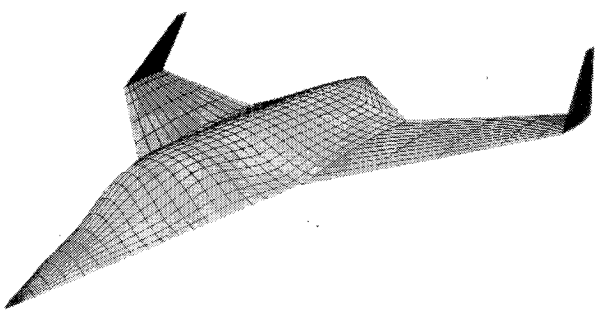

Fig. 1 Generic fighter configuration wire frame representation.

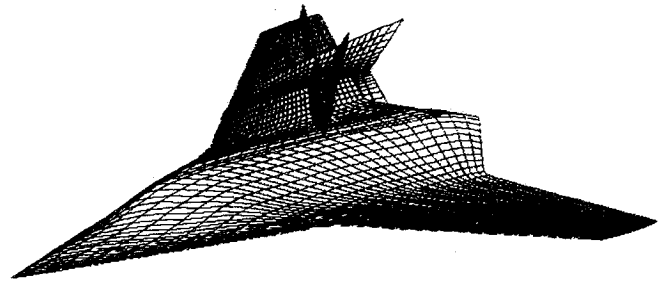

Fig. 2 Computational grid for generic fighter.

Computational Simulation Procedures

Flow simulations were performed for the generic fighter configuration using the wind-tunnel model ordinates as the surface geometry supplied to a three-dimensional wing grid generation algorithm. A single block C-H topology three-dimensional computational mesh was generated using two-dimensional numerical grid generation procedures for a series of spanwise stations starting at the root symmetry plane and progressing past the wing tip into the far field. The computational grid is illustrated in Fig. 2. The mesh employed 117 wraparound stations, 27 spanwise stations, and 32 normal stations. On the wake cut aft of the vehicle, 15 axial stations were used, whereas on the freestream tip extension past the wing tip 3 stations were employed. Uniform spacing was employed in the spanwise direction. Clustering was employed in the wraparound direction around the leading and trailing edges and in the normal direction to resolve the boundary layer. The outer computational boundary was located six fuselage lengths away from the vehicle.

The flow simulations were performed on this mesh using ENS3D executed in the steady-state full Navier-Stokes equation mode with a fully turbulent flow approximation. To achieve dynamic similitude with the experimental results, a Reynolds number of 1.25×10^6 was used in the computations, along with a freestream Mach number of 0.3. The Baldwin-Lomax algebraic turbulence model was used in the analysis. Flow computations were performed for 10-, 21-, 23-, and 25-deg angle of attack. The 10-deg case, which was also tested experimentally, corresponds to the stable vortical flow and will not be reported herein. The higher incidence cases all displayed vortex instability, with the burst onset location moving forward as the incidence was increased. The 21-deg case was studied in detail experimentally and will be discussed below. No wind-tunnel interference incidence correction was employed in the analysis. Hence, the analysis used the same geometric angle of attack as the experiment. The computational results reported below required 1200 cycles for convergence, using a uniform flow initialization of the solution.

Computed and Measured Mean Flowfield Parameters

Laser velocimeter (LV) data were collected for the 21-deg incidence case for a series of axial (x) stations. An axial station

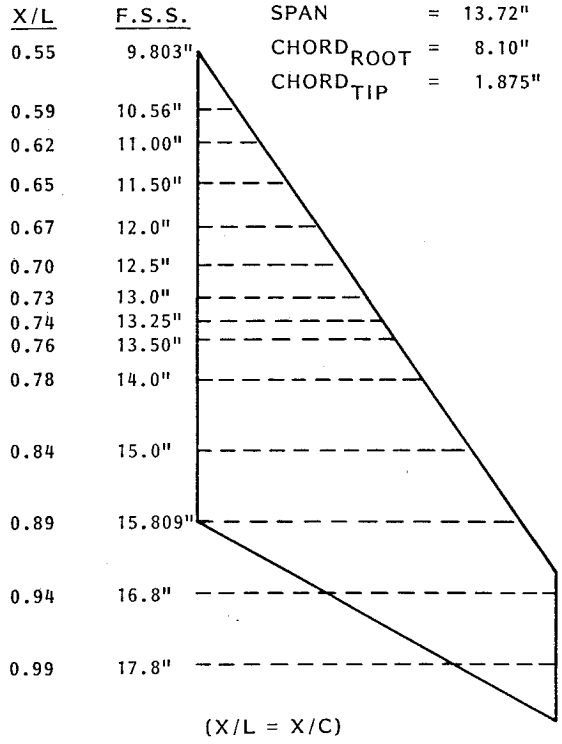

Fig. 3 LV survey axial plane designation.

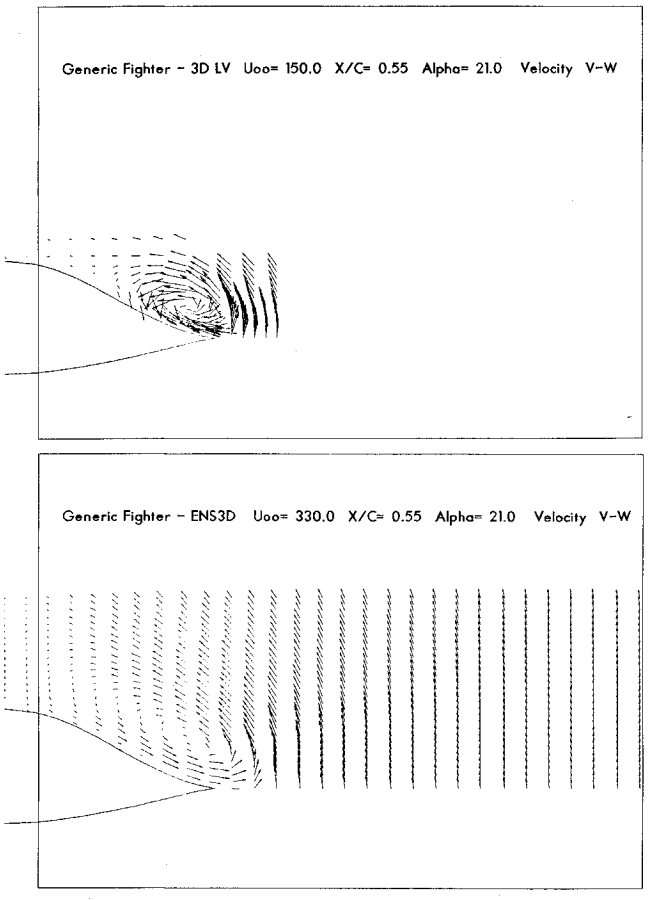

a) Results for $X/L = 0.55$

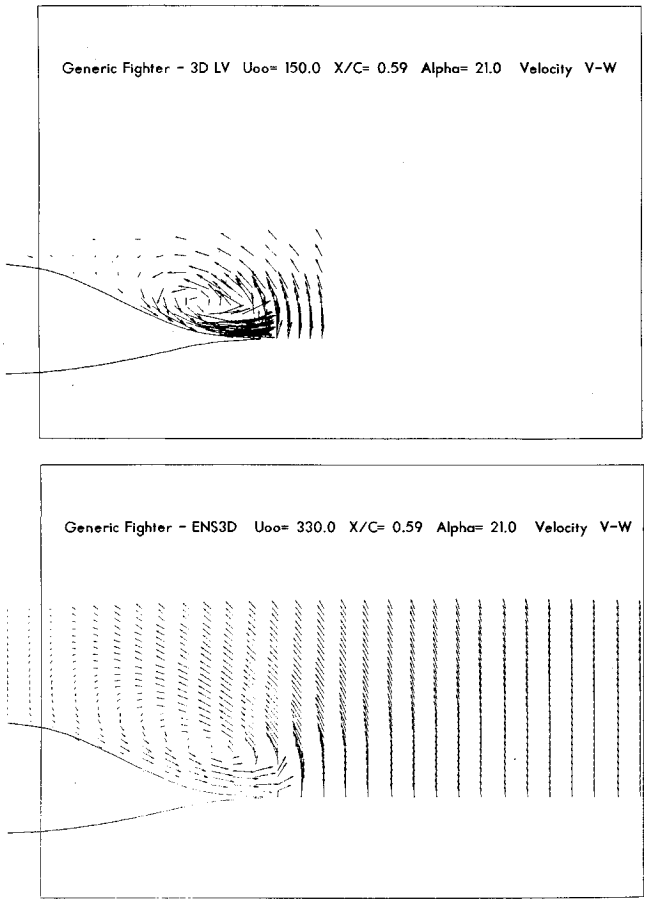

b) Results for $X/L = 0.59$

Fig. 4 Experimental and computed crossflow (y-z) velocity vector fields.

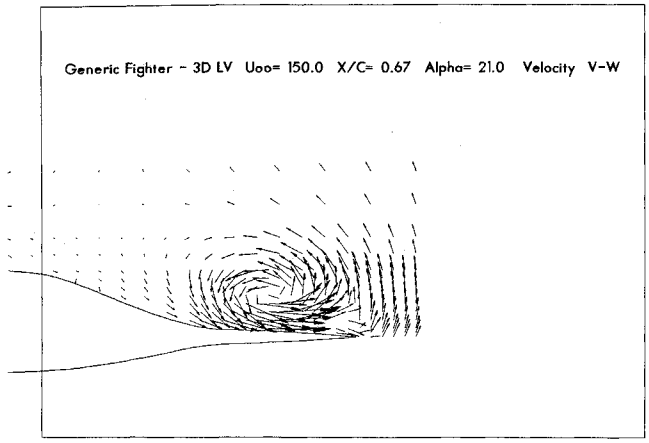

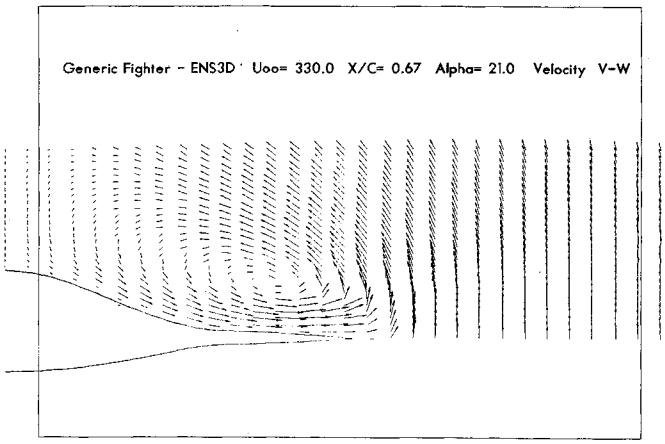

c) Results for $X/L = 0.67$

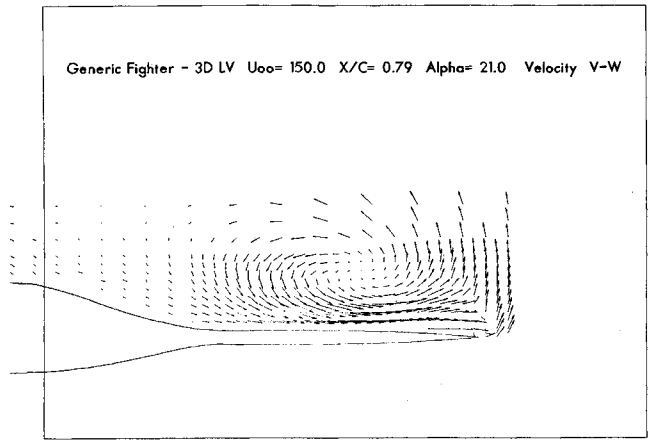

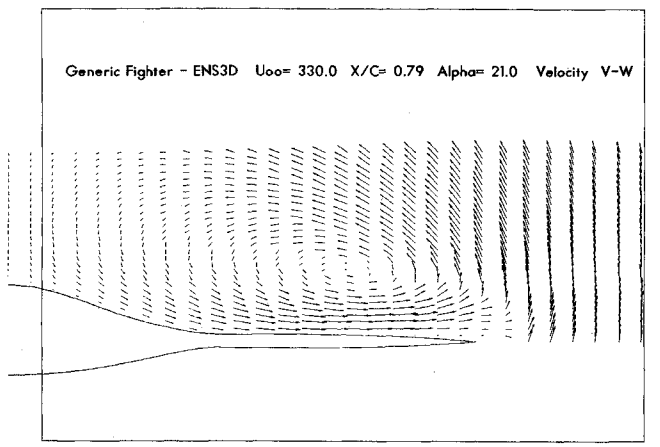

e) Results for $X/L = 0.79$

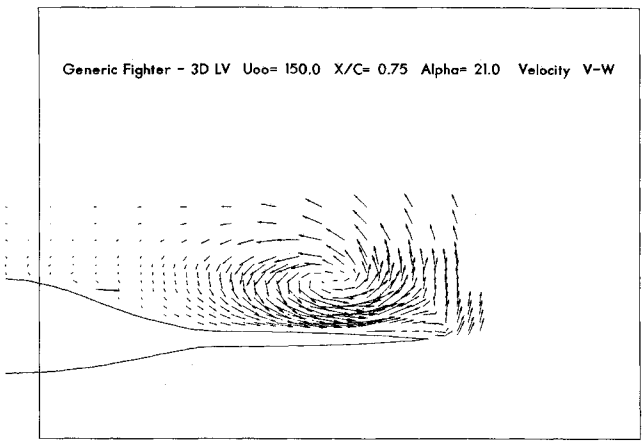

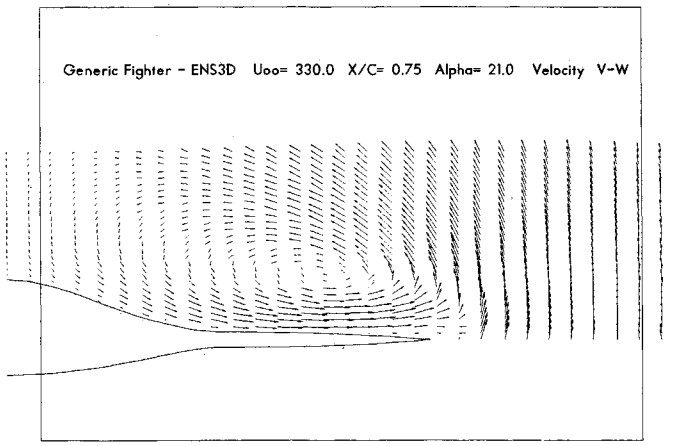

d) Results for $X/L = 0.75$

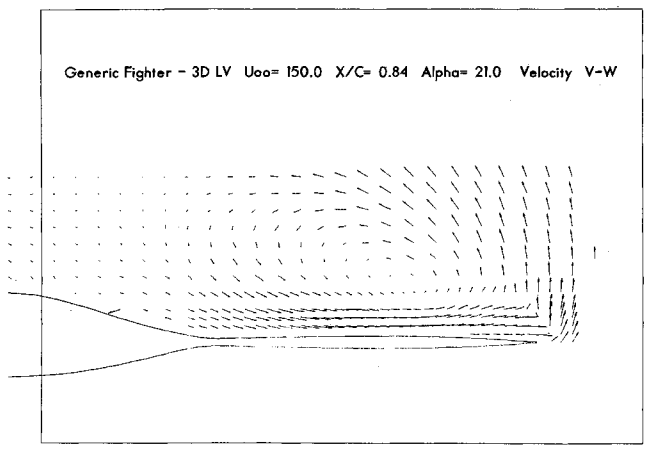

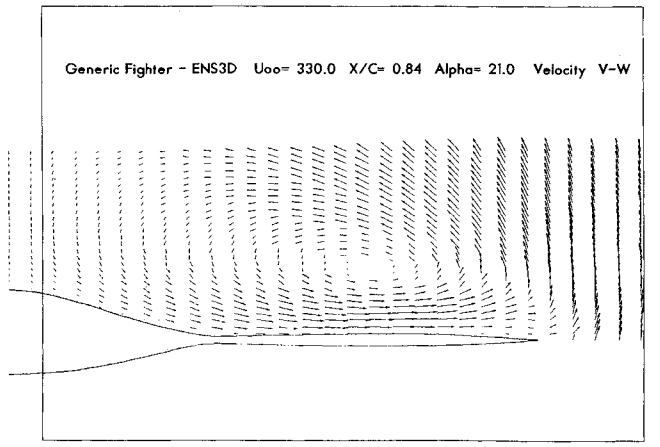

f) Results for $X/L = 0.84$

Fig. 4 (Cont.) Experimental and computed crossflow (y-z) velocity vector fields.

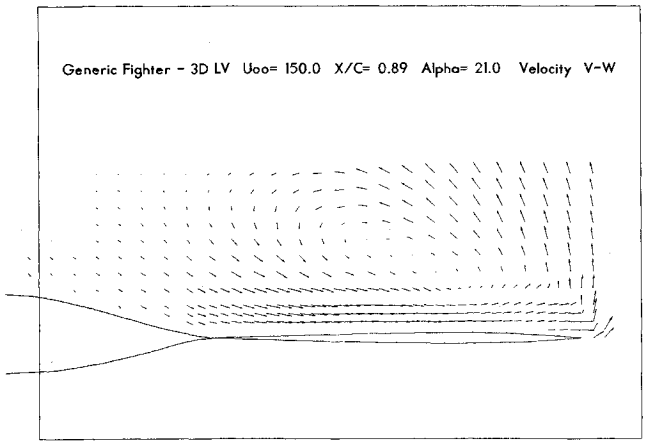

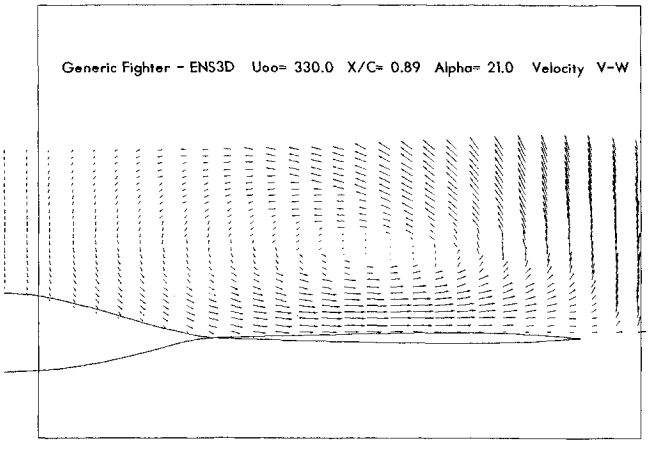

g) Results for $X/L = 0.89$

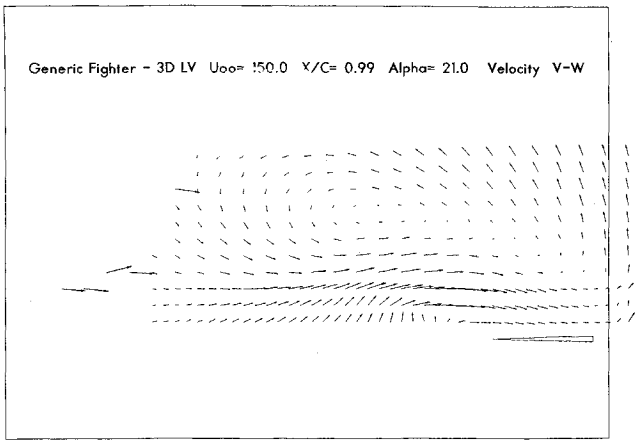

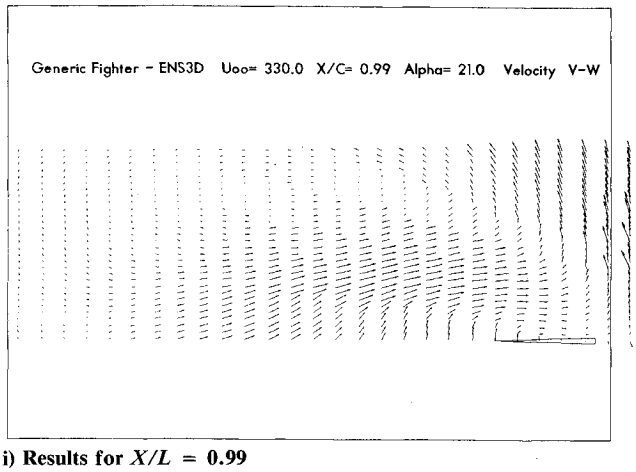

i) Results for $X/L = 0.99$

Fig. 4 (Cont.) Experimental and computed crossflow (y-z) velocity vector fields.

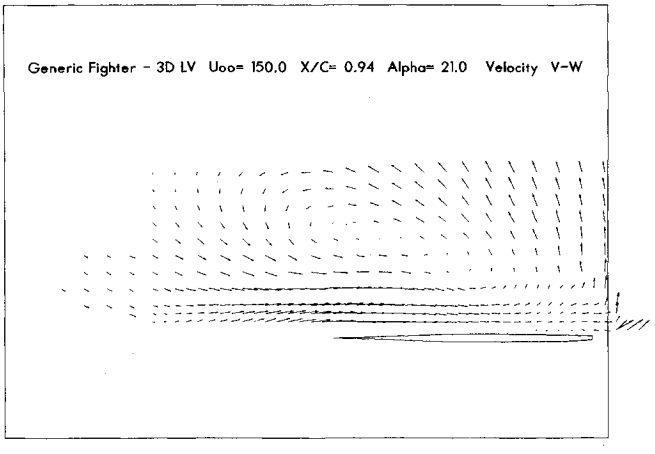

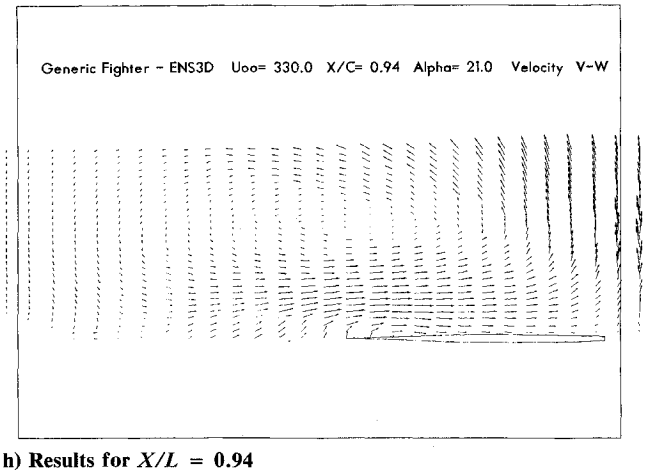

h) Results for $X/L = 0.94$

is a plane of constant x, where the x axis is the longitudinal axis of the vehicle. These stations are illustrated in Fig. 3. In this figure, x/L is the nondimensional axial position defined as the axial distance x downstream from the fuselage nose, normalized by the fuselage length L. Regions forward of the wing strake juncture and close to the model surface were inaccessible to LV surveying due to glare caused by laser beam reflections off the body.

Figure 4 presents comparisons of computed and measured crossflow (y-z) velocity fields for a series of axial (x) stations splayed along the vehicle. The computed results were interpolated from the swept-wing curvilinear grid into planes of constant x using postprocessing software. The vector origin in these plots denotes either the interpolation point for the computations or the survey point for the LV studies. The vector orientation corresponds to the local crossflow direction; its length corresponds to the local crossflow magnitude. The velocity magnitudes between the analysis and experiment have been scaled to represent approximately the same freestream velocity. The LV survey point coordinates are not the same as the interpolated computed results point coordinates.

Clearly observed in the figures is the development of a streamwise flow vortex emanating from the wing/strake junction region. This vortex initially begins to traverse the wing in the spanwise direction, while at the same time the height of the vortex core increases with increasing x/L location. For the upstream axial stations, the vorticity strength is high (high swirl). At the aft stations ($x/L \geq 0.84$), the swirl magnitude appears to diminish rapidly, indicating a loss in vortex strength and suction. As will be shown shortly, this loss in vortex strength is associated with the onset of vortex burst and with the formation of an inflow stagnation point.

Figure 5 presents the computed and experimentally observed paths of the vortex core on the upper wing surface for the 21-deg incidence case. Also shown is the path of the vortex core for the 10-deg case. For the 10-deg case, the vortex continually translates outward along the wing span as the axial position is increased. This case corresponds to a stable nonburst vortex, as is experimentally observed. For the 21-deg incidence case, however, the vortex core translates outward along the wingspan to about wing midchord, at which point it convects aftward along the streamwise direction. This phenomenon is associated with the onset of burst and subsequent mitigation in vorticity magnitude.

The computational analysis provides as output the three Cartesian velocity components, static pressure, static temperature, density, Mach number, total pressure, and total temperature at each mesh point. Shown in Fig. 6 are the computed upper-wing static nondimensional pressure fields at three successive chordwise grid stations on the vehicle, as viewed from ahead of the vehicle. (These chordwise grid stations are aligned with the wing sweep and are not orthogonal to the x axis. They follow the surface spanwise grid lines shown in Fig. 2.) The upper-wing pressure field figures are presented in contour format. The nondimensional pressure is defined as the local static pressure normalized by the product of the freestream density and the sonic speed squared. For this case, 0.71 is freestream pressure. The contour scales for each of the figures are the same, although the latter two figures are geometrically scaled to a slightly reduced horizontal span. At the forward grid station ($I=70$), a high vortex strength is observed with high suction (reduced pressure) at the vortex core. At the next grid station ($I=80$), which is aft of the previous station,

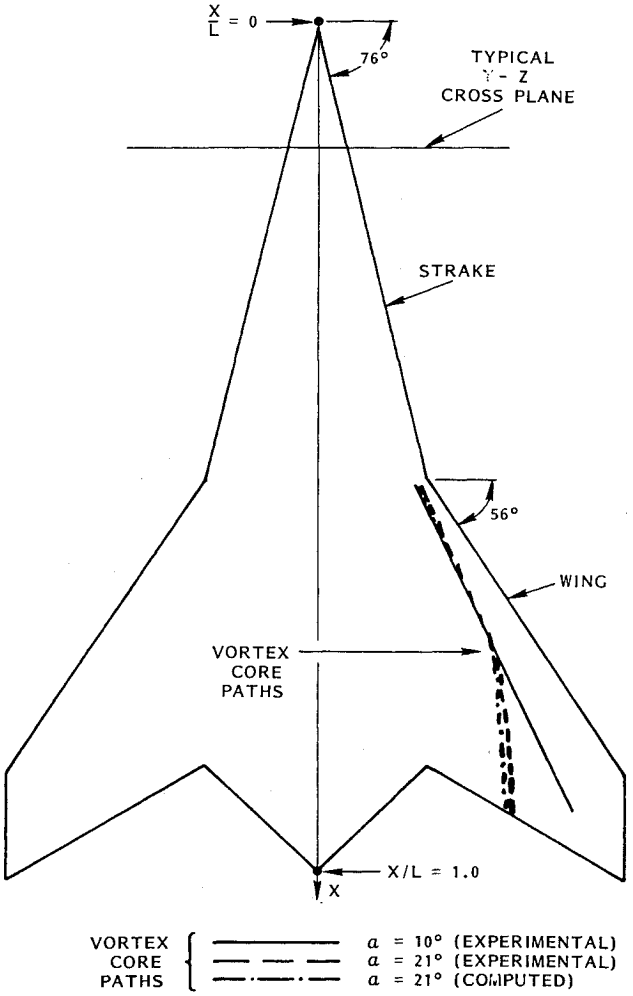

Fig. 5 Experimental and computed vortex core paths for 10-deg and 21-deg incidence cases.

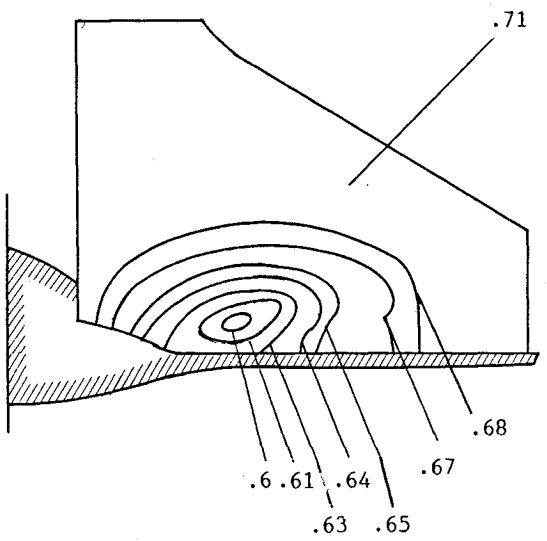

a) Pressure field for station I = 70

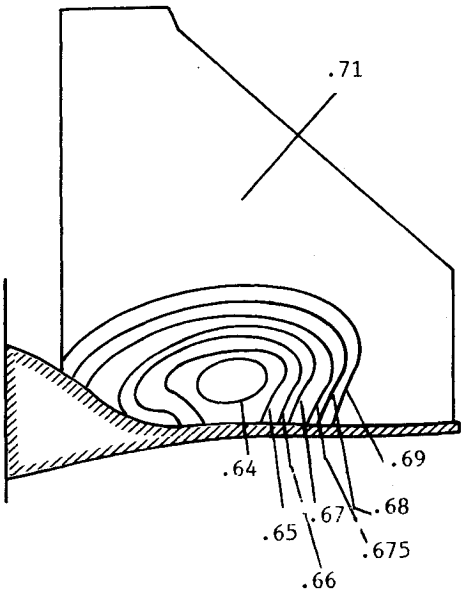

b) Pressure field for station I = 80

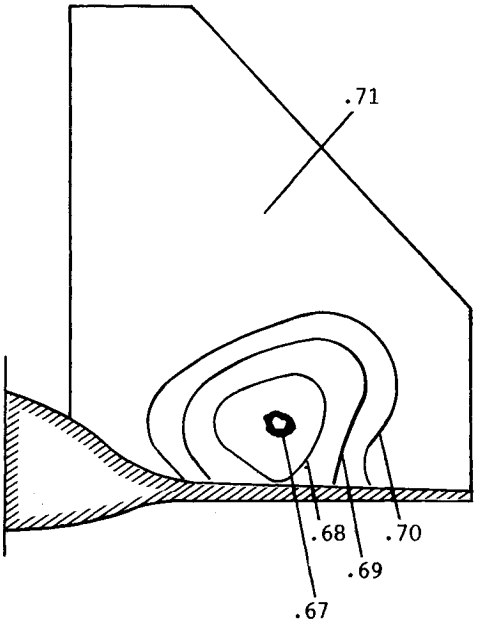

c) Pressure field for station I = 90

Fig. 6 Computed chordwise grid station static pressure fields for 21-deg incidence case.

the vortex core has moved out along the wing span and has increased in height. Along with this displacement of the core location is a mitigation in vortex strength as evidenced by an increase in the core static pressure level and reduced suction. This displacement of the core position and reduction in vortex strength is continued as grid station ($I=90$) is reached, which is still further aft. After the vortex burst, however, the remaining portion of the vortex core is convected in a nearly downstream direction, as shown earlier.

In addition to surveying the crossflow (y-z) velocity components, the three-dimensional LV system can also determine the axial (x) velocity component field. The results of the LV axial velocity survey for a number of axial stations (stations of constant x) are shown in Fig. 7 for the 21-deg incidence case. This is an isometric contour map (as viewed from aft of the vehicle) where the freestream velocity components have been eliminated. Also shown in the figure is the planform (and sections) of the vehicle. The highest axial velocity is obtained in the vortex core region at the upstream axial stations. In moving aft, however, the vortex core axial velocity components become reversed, indicating an in-flow stagnation point. This indicates vortex breakdown above the wing's surface at the location where the axial component of velocity is first seen to be reversed. Downstream from the stagnation point, a cigar-shaped region of reversed flow is seen above the wing. The downstream stagnation point is located near the 96% chord survey location. A similar type of situation is reported by Leuchter and Solignac,[17] where reversed axial flow at the vortex core was detected.

Similar LV surveys were taken for the 10-deg incidence case and no reversed axial flow was detected, indicating a stable nonburst vortical flowfield for that case.

Figure 8 illustrates ENS3D computed axial velocity contours for the 21-deg incidence case. This figure shows the streamwise isotachs (lines of constant x velocity) for chordwise grid stations on the wing upper surface (these surfaces are not planes of constant x but rather are aligned with the spanwise surface grid lines shown in Fig. 2). At the first grid station illustrated, the reversed axial flow region has just begun to indicate burst onset. At the second grid station, the extent of reversed axial flow has increased considerably. Detailed comparison of the x/L locations of the onset of vortex burst has indicated that the location predicted by the analysis is slightly aft of that observed experimentally.

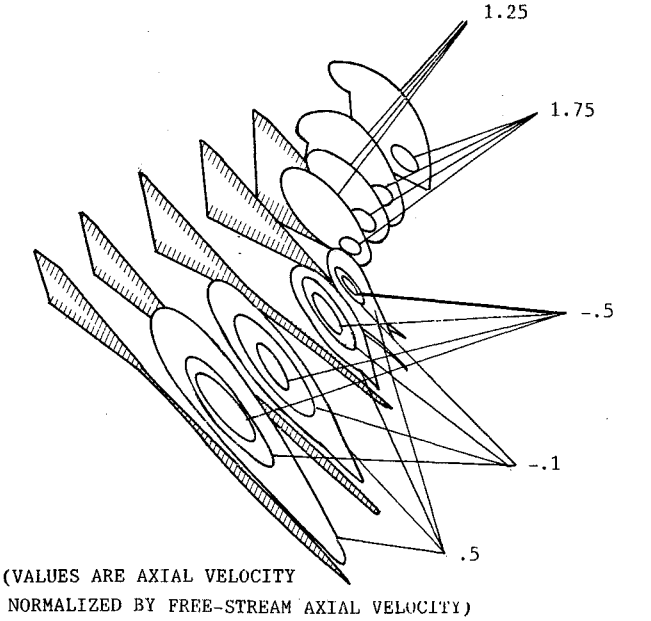

Fig. 7 Experimental axial station axial velocity contours for 21-deg incidence case.

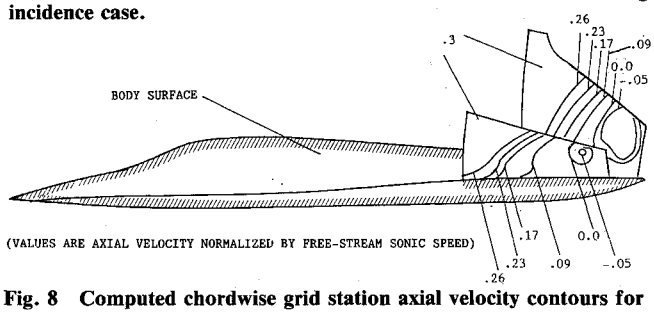

Fig. 8 Computed chordwise grid station axial velocity contours for 21-deg incidence case.

This difference can be attributed to a number of causes, including insufficient mesh resolution, turbulence modeling, transition onset specification (flow assumed fully turbulent), and lack of incidence correction in the analysis to account for wind-tunnel blockage effects. Moreover, in performing the LV survey studies it was noted that a small temporal variation existed in the burst onset axial position indicating a nonsteady type of behavior for the 21-deg incidence case.

A limited study was conducted in adjusting the computational grid to determine what effect this had on the computed vortex breakdown results. This study was confined to maintaining the same total number of grid points, since this number was constrained because of computer memory limitations (four million words of storage). Alteration of the grid clustering parameters to concentrate a few more chordwise grid stations in the vortex burst region did not produce any pronounced effects on the computed burst onset location; it was still slightly aft of that noted experimentally. It was also noted that the computed vortex core vorticity levels were below those measured for the region ahead of vortex breakdown. If a substantially denser mesh were to be used, this might improve the predicted burst onset location and the vortex core vorticity levels ahead of breakdown.

As mentioned previously, a fully turbulent flow approximation was made and the two-layer Baldwin-Lomax turbulence model was employed in performing the simulations. Although the analysis has the capability to use streamwise eddy viscosity relaxation in conjunction with this model, this option was not employed in this study. The analysis also has the option to use the k-ϵ turbulence model, which is based on solving two additional partial differential equations for the turbulent kinetic energy k and the turbulence dissipation rate ϵ. In the experimental testing effort,[9] it was noted that the turbulent kinetic energy maximized just ahead of the vortex breakdown location. Time constraints in the present study did not allow the k-ϵ model to be employed, although it would be enlightening to observe if it also shows a maximum in k ahead of burst onset.

Conclusions

Analytical and experimental investigations have been performed for the vortical flowfield about a generic fighter configuration operating at sufficiently high incidence to cause vortex breakdown. The analytical predictions, based on solutions of the full Reynolds-averaged Navier-Stokes equations, are in accordance with the experimentally measured laser velocimeter results. It is felt that with further mesh and turbulence model refinement and the corresponding experimental effort to extend the validation data base, a method to estimate loads due to vortex-airframe interaction can be developed.

Acknowledgment

The experimental data base referred to herein was acquired by C. J. Novak and C. R. Huie. Their efforts are gratefully acknowledged. This work was supported by the Lockheed Independent Research and Development Program.

References

[1]Wentz, W. H., "Vortex-Fin Interaction on a Fighter Aircraft," AIAA Paper 87-2474, Aug. 1987.

[2]Campbell, J. F., and Osborn, R. F., "Leading Edge Vortex Research: Some Nonplanar Concepts and Current Challenges,"

NASA CP-2416, Oct. 1985.

[3]Rizzetta, D. P., and Shang, J. S., "Numerical Simulation of Leading Edge Vortex Flows," *AIAA Journal*, Vol. 24, No. 2, 1986, pp. 237–245.

[4]Buter, T. A., and Rizzetta, D. P., "Steady Supersonic Navier-Stokes Solutions of a 75° Delta Wing," NASA CP-2416, Oct. 1985.

[5]Newsome, R., and Thomas, J. L., "Computation of Leading-Edge Vortex Flows," NASA CP-2416, Oct. 1985.

[6]Fujii, K., and Schiff, L. B., "Numerical Simulation of Vortical Flows over a Strake-Delta Wing," *AIAA Journal*, Vol. 27, No. 9, 1989, pp. 1153–1162.

[7]Murman, E. M., Powell, K. G., Miller, D. S., and Wood, R. M., "Comparison of Computations and Experimental Data for Leading Edge Vortices—Effects of Yaw and Vortex Flaps," AIAA Paper 86-0439, Jan. 1986.

[8]Thomas, J. L., and Newsome, R. W., "Navier-Stokes Computations of Lee-Side Flow over Delta Wings," AIAA Paper 86-1049, May 1986.

[9]Novak, C. J., and Huie, C. R., "3-D Laser Velocimeter Investigations of a Generic Fighter Flowfield," AIAA Paper 87-0331, Jan. 1987.

[10]Yee, H. C., and Harten, A., "Implicit TVD Schemes for Hyperbolic Conservation Laws in Curvilinear Coordinates," *AIAA Journal*, Vol. 25, No. 2, 1987, pp. 266–274.

[11]Baldwin, B. S., and Lomax, H., "Thin Layer Approximation and Algebraic Model for Separated Turbulent Flows," AIAA Paper 78-257, Jan. 1978.

[12]Gorski, I. J., "A New Near-Wall Formulation for the k-ϵ Equations of Turbulence," AIAA Paper 86-0556, Jan. 1986.

[13]Vadyak, J., Smith, M. J., and Schuster, D. M., "Navier-Stokes Simulations of Supersonic Fighter Intake Flowfields," AIAA Paper 87-1752, June 1987.

[14]Vadyak, J., Smith, M. J., Schuster, D. M., and Weed, R. M., "Simulation of External Flowfields Using a 3-D Euler/Navier-Stokes Algorithm," AIAA Paper 87-0484, Jan. 1987.

[15]Vadyak, J., Smith, M. J., Schuster, D. M., and Shrewsbury, G. D., "Simulation of Aircraft Component Flowfields Using a Three-Dimensional Navier-Stokes Algorithm," 3rd International Symposium on Science and Engineering on Cray Supercomputers, Cray Research, Inc., Minneapolis, MN, Sept. 9–11, 1987.

[16]Vadyak, J., and Smith, M. J., "Simulation of Engine Installation Flowfields Using a Three-Dimensional Euler/Navier-Stokes Algorithm," AIAA Paper 86-1537, June 1986.

[17]Leuchter, O., and Solignac, J. L., "Experimental Investigation of the Turbulent Structure of Vortex Wakes," ONERA TP-1983-107, Sept. 1983.